Unlocking High Capacity and Reversible Alkaline Iron Redox using Silicate-Sodium Hydroxide Hybrid Electrolytes

Sathya Narayanan Jagadeesan,[a] Fenghua Guo,[b] Ranga Teja Pidathala,[c] A.M. Milinda Abeykoon,[d] Gihan Kwon,[d] Daniel Olds,[d] Badri Narayanan,[c] and Xiaowei Teng [a]**

[a] Department of Chemical Engineering, Worcester Polytechnic Institute, 100 Institute Road, Worcester, MA 01609, United States.

[b] Department of Chemical Engineering, University of New Hampshire, 33 Academic Way, Durham, NH 03824, United States.

[c] Department of Mechanical Engineering, University of Louisville, 332 Eastern Pkwy, Louisville, Kentucky 40292, United States.

[d] National Synchrotron Light Source II, Brookhaven National Laboratory, 743 Brookhaven Avenue, Upton, New York 11973, United States.

* Correspondence to: xteng@wpi.edu, and badri.narayanan@louisville.edu

Keywords: alkaline iron batteries, electrolyte additives, silicates, *operando* x-ray diffraction, molecular dynamics modeling,

Abstract

Alkaline iron (Fe) batteries are attractive due to the high abundance, low cost, and multiple valent states of Fe but show limited columbic efficiency and storage capacity when forming electrochemically inert Fe_3O_4 on discharging and parasitic H_2 on charging. Herein, sodium silicate is found to promote $Fe(OH)_2$/FeOOH against $Fe(OH)_2$/Fe_3O_4 conversions. Electrochemical experiments, *operando* X-ray characterization, and atomistic simulations reveal that improved $Fe(OH)_2$/FeOOH conversion originates from (i) strong interaction between sodium silicate and iron oxide and (ii) silicate-induced strengthening of hydrogen-bond networks in electrolytes that inhibits water transport. Furthermore, the silicate additive suppresses hydrogen evolution by impairing energetics of water dissociation and hydroxyl de-sorption on iron surfaces. This new silicate-assisted redox chemistry mitigates H_2 and Fe_3O_4 formation, improving storage capacity (199 mAh g^{-1} in half-cells) and coulombic efficiency (94% after 400 full-cell cycles), paving a path to realizing green battery systems built from earth-abundant materials.

1. Introduction

The high energy density and exceptional cycle life of lithium-ion batteries (LIBs) based on intercalation chemistry have enabled rapid advances in the commercialization of electric vehicles and portable electronics [1]. However, flammable electrolytes and increasing costs of critical materials have raised concerns for large-scale implementation of LIBs in stationary storage [2, 3]. Aqueous metal-ion batteries (MIBs) using aqueous electrolytes, earth-abundant materials, and metal-air and metal-sulfur chemistries show great promise in grid storage by alleviating manufacturing costs and safety concerns [4-7]. Among various MIBs, alkaline iron (Fe) batteries are attractive due to several merits of Fe materials, such as the multiple electrons transfer redox, high abundance in the earth's crust, low toxicity, and good geographic accessibility [8]. Moreover, alkaline Fe batteries have two unique features superior to other battery systems. Firstly, Fe is biodegradable, less toxic, and more environmentally friendly than other metals, and thus, alkaline Fe batteries may have a smaller environmental footprint throughout their lifecycle, making them perfect for large-scale grid storage. Secondly, the redox forms of iron materials, including $Fe(OH)_2$, Fe_3O_4, Fe_2O_3, and FeOOH, have very low solubility in water. Thus, dendrite formation, one of the most severe issues that need to be addressed in most battery systems (including alkaline Zn batteries), is much less probable in alkaline Fe battery systems [9, 10]. However, the Fe redox exhibits poor coulombic efficiency and limited storage capacity, mainly due to Fe_3O_4 and H_2 formation during the discharge and charge processes [11, 12] Some successes have been reported in mitigating the hydrogen evolution reaction (HER) during the $Fe(OH)_2 \rightarrow Fe$ charge process by forming FeS interphase on the electrode surface [13, 14]. However, the chemical instability of FeS interphase during discharging raises concerns over its long-term effects on HER inhibition.

Recently, authors reported that anion-insertion facilitated $Fe(OH)_2$/FeOOH conversion via forming anions (e.g., SO_4^{2-} or Cl^-) intercalated $Fe(OH)_2$ [15, 16], also called green rust (GR), $[Fe^{2+}_{1-x}Fe^{3+}_x (HO^-)_2]^{X+} (A^{n-}_{x/n})^{X-}$, where anions ($A^{n-}$) are intercalated between the Fe-O interlayers. Thus, Fe^{2+}/Fe^{3+} conversion could proceed under GR layered structure without forming a close-packed Fe_3O_4 phase. The anion-insertion-assisted $Fe(OH)_2$/FeOOH redox leads to a more efficient discharge pathway in Fe redox. However, Fe_3O_4 remained the major discharge product since the sluggish anion transport limited the formation of the GR phase upon discharge. Moreover, this anion-insertion redox chemistry cannot enable a more efficient Fe charging chemistry, where parasitic hydrogen evolution impairs the coulombic efficiency and impedes the realization of the full potential of alkaline Fe batteries.

Optimizing the electrode and electrolyte interplay to tailor the redox chemistry has been essential in battery research. Some strategies, including electrolyte additives, artificial coating, and solid electrolyte interphase (SEI), have been successfully adopted to improve the electrochemical behaviors during the charge transfer process [17-19]. Controlling electrolyte additives is probably the most scalable approach due to the simple preparation process and ease of scale. Successful examples include Water-in-Salt Electrolytes (WiSE) to improve the stability of aqueous electrolytes for expanded voltage windows [20, 21]. WiSE is prepared by dissolving high concentrations of salts (usually higher than 20 M) in aqueous electrolytes. It reduces water activity (e.g., fewer "free water" molecules in the electrolyte since most water molecules are solvated with salt ions) and helps form fluorinated SEIs to prevent Li from reacting with water. Recently, hybrid solvents were reported as a promising design for Li-ion and Zn-ion aqueous batteries, where a portion of the water was substituted by alcohols, such as polyethylene glycol (PEG) [22, 23], The additives function as molecular crowding agents (MCAs) to confine water molecules via hydrogen bonding to decrease the water activity, a different working mechanism from WiSE. Unfortunately, the polyol nature of PEGs makes them electrochemically reactive during the cathodic reaction. Besides alcohol, sulfolane is a new type of highly stable MCA in aqueous Li-ion and Zn-ion batteries, offering an expanded electrochemically stable voltage window for water and forming fully hydrated cations for enhanced transport [24-26]. However, the polar aprotic nature of sulfolane challenges the formation of stable electrolytes with alkaline battery systems.

While WiSE and MCA successfully alter the water activity and solvation behavior of cations, there is no report on how electrolyte additives tune the Fe redox chemistry in alkaline electrolytes, where hydroxyl anions play essential roles in the redox behaviors and alkali cations (e.g., Na^+, K^+) seldom participate in the charge-transfer process. Moreover, remedying the effects of WiSE and MCA requires large quantities, which might impede large-scale implementation due to the high cost of concentrated additives. Therefore, developing new approaches to suppress HER at charging and promote FeOOH formation at discharging are ongoing challenges to realize Fe alkaline batteries for low-cost and long-duration electricity storage applications [15, 27]. Sodium silicate (Na_2SiO_3) is highly stable and soluble in neutral and alkaline solutions, which was first patented in the 1960s to passivate metal surfaces, preventing iron, steel, copper, and brass from corrosion when combined with zinc sulfate [28, 29]. Inspired by this phenomenon in corrosion research, we design and demonstrate that highly diluted Na_2SiO_3 in the parts per million (ppm) level can be an effective MCA in alkaline solutions to reduce water activity in alkaline Fe batteries. Intriguingly, Na_2SiO_3 has

two folds effectiveness on Fe-redox: (i) on charging (reduction process), it interacts with water by strengthening hydrogen bond (HB) networks to suppress $Fe(OH)_2$→Fe conversion and block H_2O→H_2 evolution on Fe surface; (ii) its passivation effect on $Fe(OH)_2$→Fe conversion allows a lower reduction potential on charging to improve $Fe(OH)_2$ formation, which, in turn, benefits $Fe(OH)_2$→FeOOH conversion on discharging with nearly six times of improved discharge capacity compared to the electrolyte without Na_2SiO_3 additives.

2. Results

2.1. Hydrogen bonding and water transport in hybrid electrolytes by reactive molecular dynamics simulation

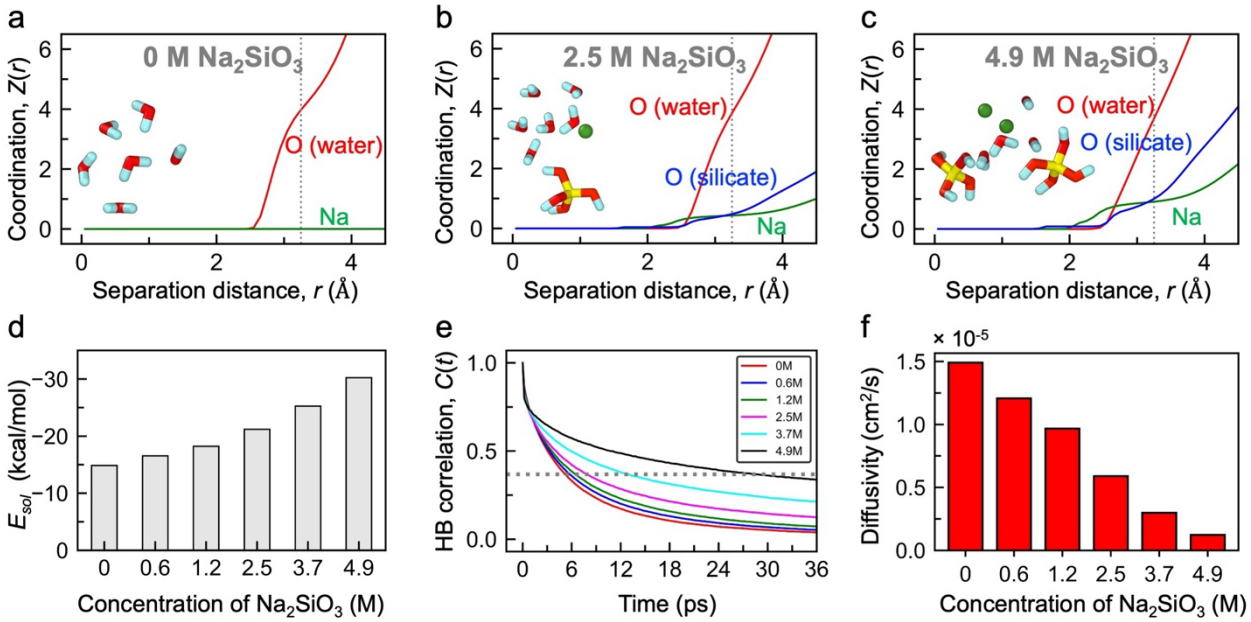

Figure 1. Reactive molecular dynamics simulations. (a-c) Atomic coordination number, $Z(r)$, of O from water (red), O from silicate species, namely SiO_3^{2-}, $H_xSiO_4^{(4-x)-}$, and $Si(OH)_4$ (blue), as well as Na^+ (green) around water in 0.01 M NaOH solution with various concentrations of Na_2SiO_3. The dotted line denotes the first solvation shell at 3.25 Å. The atomic configuration of the representative first solvation shell around water is shown as an inset, where Na, Si, O, and H atoms are in green, yellow, red, and aqua, respectively. (d) The average energy of interactions (E_{sol}) between water and the molecules in the first solvation shell. (e) Hydrogen bond correlation function $C(t)$ in electrolytes at different Na_2SiO_3 concentrations. The grey dotted line refers to $C=1/e$ and indicates the lifetime of the hydrogen bond network in water. (f) Diffusivity of water at different Na_2SiO_3 concentrations.

Reactive molecular dynamics (RMD) simulations elucidate the effect of silicate additives on strengthening the hydrogen bonding (HB) network and limiting water transport in Na_2SiO_3/NaOH solutions relative to NaOH solution (**Figure 1**). Similar to previous works on silicate/water systems [30], RMD simulations indicate that most SiO_3^{2-} anions combine with OH^- and H^+ ions from water/NaOH to form $Si(OH)_4$ molecules, especially at low silicate concentrations (**Figure S1**). Interestingly, in addition to $Si(OH)_4$, we also observe a significant amount of $H_xSiO_4^{(4-x)-}$species (x = 1– 4), as well as preserved SiO_3^{2-} in the

electrolyte, regardless of the Na_2SiO_3 concentration (**Figure S1**). For instance, at ~0.6 M Na_2SiO_3, ~67% of the silicate anions form $Si(OH)_4$, while the remaining exist as $H_3SiO_4^-$ (~25%), $H_2SiO_4^{2-}$ (~6%), $HSiO_4^{3-}$ (~1%), and preserved SiO_3^{2-} (~1%) species (**Figure S1**). The relative fraction of $H_xSiO_4^{(4-x)-}$ and intact SiO_3^{2-} species rises steadily with increase in Na_2SiO_3 concentration, at the expense of $Si(OH)_4$; yielding a more uniform distribution of $Si(OH)_4$ (~26%), $H_3SiO_4^-$ (~40%), $H_2SiO_4^{2-}$ (~20%), $HSiO_4^{3-}$ (~6%), and preserved SiO_3^{2-} (~8%) species at 4.9 M Na_2SiO_3 (**Figure S1**).

We evaluated the atomic coordination number around water, $Z(r)$, as a function of separation distance, r, obtained by integrating the radial distribution functions over the last 1 ns of RMD trajectories of 0.01 M NaOH aqueous solution with varying amounts of Na_2SiO_3 (0 – 4.9 M) equilibrated under ambient conditions (**Figures 1a-c**). In the absence of Na_2SiO_3 (i.e., 0.01 M NaOH aqueous solution), each water molecule prefers to coordinate with ~4 other water molecules in its first solvation shell via hydrogen bonds, nearly identical to that observed in pure liquid water (**Figure 1a**) [30]. Upon the addition of Na_2SiO_3, silicate species (i.e., SiO_3^{2-}, $H_xSiO_4^{(4-x)-}$, and $Si(OH)_4$), and Na^+ cations begin to appear in the first solvation shell, averaging ~0.5 silicate species and ~0.5 Na^+ neighbors at 2.5 M Na_2SiO_3, respectively (**Figure 1b**). The average number of Na^+ and silicate species in the first solvation shell increases progressively with Na_2SiO_3 concentration, averaging ~one silicate species and one Na^+ neighbor at 4.9 M Na_2SiO_3 (**Figure 1c**). Notably, the number of water molecules in the first solvation shell remains nearly constant (~4) at all Na_2SiO_3 concentrations (**Figures 1a-c**). The increased presence of Na^+ and silicate species near water enhances the energetic stability of the solvation clusters at the higher Na_2SiO_3 concentrations, indicated by increasing (more negative) solvation energy from -15 to -30 kcal/mol when Na_2SiO_3 concentrations increased from 0 to 4.9 M (**Figure 1d**).

To assess the effect of the energetics of the solvation cluster on the dynamics of the HB network, we evaluated the HB correlation function, $C(t)$, using a well-established method (Details in Methods section) [31]. The lifetime of the HB network in water, τ, is defined such that $C(\tau) = 1/e$ [30]. As expected, the HB lifetime in electrolytes without Na_2SiO_3 additive is ~5 ps, similar to pure liquid water. In electrolytes containing Na_2SiO_3, the lifetime of the HB network is directly correlated with the stability of the solvation cluster, with an appreciably higher lifetime observed at high Na_2SiO_3 concentrations that feature more stable solvation clusters (4.9 M: τ ~30 ps; 0.6 M: τ ~6 ps). The dynamics of rearrangement of the HB network – critical for molecular transport of water – is significantly impeded in electrolytes containing

Na_2SiO_3. Indeed, the calculated diffusivity of water in hybrid electrolytes containing Na_2SiO_3 is significantly lower (up to 1 order of magnitude in 4.9 M Na_2SiO_3) than in NaOH electrolytes (**Figure 1f**), suggesting the capability of Na_2SiO_3 as an MCA in an alkaline electrochemical system.

2.2. Electrochemistry of Fe^{2+}/Fe^{3+} conversion in NaOH/Na_2SiO_3 hybrid electrolytes

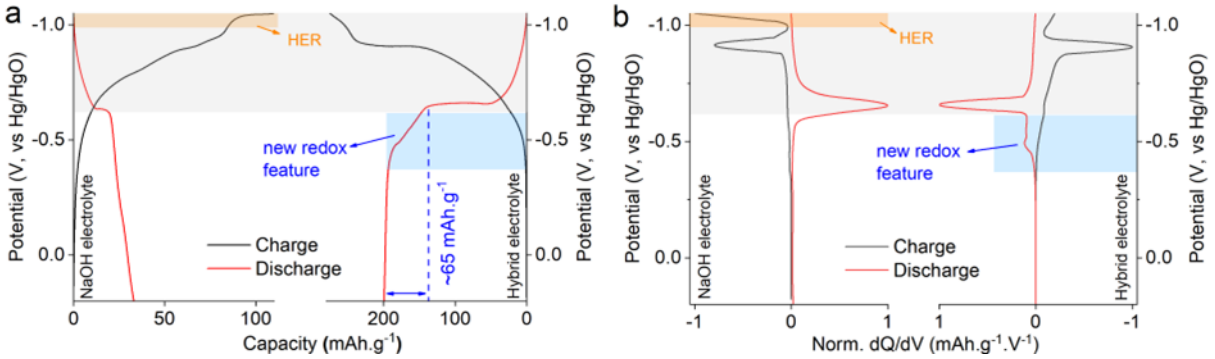

Figure 2. Electrochemical investigations. (a) CP curves of iron oxides at the current density of 0.1 A g^{-1} from 0.2 V to -1.05 V and (b) corresponding dQ/dV curves. Both plots highlight the additional redox features attributed to HER in the NaOH electrolyte and other discharge features in the hybrid electrolyte.

Iron oxides were selected as representative anode materials to investigate Fe redox electrochemistry in NaOH/Na_2SiO_3 hybrid electrolytes. Scanning electron microscopy image shows iron oxide materials have a morphology of a combination of nanoparticles (average diameter of ~50 nm) and nanorods (average width of ~40 nm and length of ~150 nm) (**Figure S2**). **Figure S3a** shows synchrotron X-ray diffraction (XRD) of iron oxides containing goethite (α-FeOOH, JCPDS: 00-100-8767) and magnetite (Fe_3O_4, JCPDS: 00-900-2673) with a molar fraction of 75.5% and 24.5% (based on total Fe atoms) from the Rietveld refinement. X-ray photoelectron spectroscopy (XPS) Fe-2p spectra show a binding energy gap of 13.6 eV between Fe $2p_{1/2}$ and $2p_{3/2}$, confirming mixed Fe^{2+} and Fe^{3+} valence states of materials (**Figure S3b**) [32, 33].

Figure 2a shows chronopotentiometry (CP) curves of iron oxides measured in NaOH (0.01 M) and NaOH/Na_2SiO_3 (0.01 M/150 ppm) hybrid electrolytes at the current density of 0.1 A g^{-1} between 0.2 V and -1.05 V (vs. Hg/HgO) in a half-cell. **Figure 2b** depicts the 1st order derivative of capacity to voltage (dQ/dV), calculated from the CP curves. In the NaOH electrolyte, iron oxides show a single charging plateau at -0.91 V and a discharging plateau at -0.65 V, exhibiting a discharge capacity of 33 mAh g^{-1}. In the hybrid electrolyte, discharge capacity increased to 199 mAh g^{-1}, six times higher than the NaOH electrolyte. Unlike the single discharge and charge plateau in NaOH (attributed to $Fe(OH)_2/Fe_3O_4$ conversion evidenced by *operando* XRD), CPs in hybrid electrolytes show an additional charging plateau

at ~ -0.51 V and a discharging plateau at ~ -0.48 V (attributed to $Fe(OH)_2$/FeOOH conversion). This new redox feature is also observed in the dQ/dV curve and accounts for an additional discharge capacity of ~ 65 mAh g^{-1}, strongly suggesting the improved Fe^{2+}/Fe^{3+} conversion. The unique plateau in the NaOH electrolyte at -1.05 V (**Figures 2a-b**) is attributed to HER (see more discussion in **Figure 7**). **Figure S4** shows the first six cycles of CP curves in both electrolytes, their capacity ratios, and dQ/dV, highlighting other redox conversions. The contribution of $Fe(OH)_2$/FeOOH conversion to overall capacity improved in the hybrid electrolyte, suggesting encouraging FeOOH formation and discouraging Fe_3O_4 formation improved the cycle stability of the iron oxide redox system.

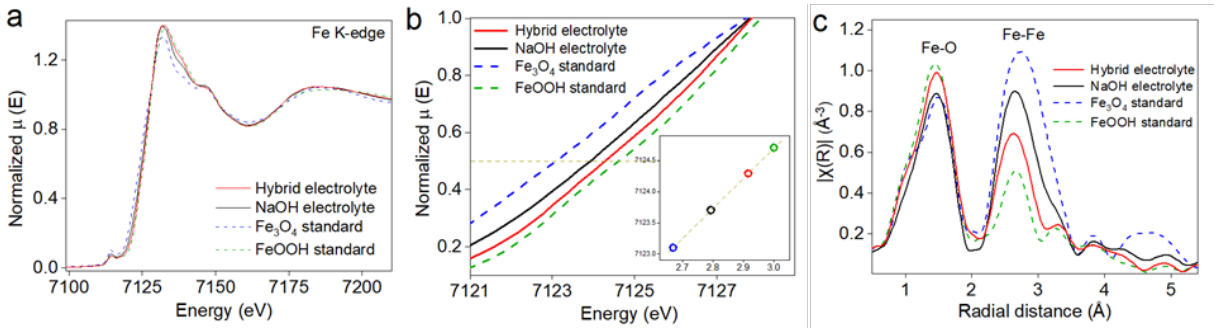

Figure 3. XAS studies of valence states of the discharged materials. (a) XAS analysis of fully discharged iron oxides (0.2 V) at Fe K-edge in NaOH and hybrid electrolytes compared with the Fe_3O_4 and FeOOH standards. (b) Zoom-in XAS spectra showing the energy shift at ½μE with the inset of the linear fit of Fe valence states. (c) Fourier Transform of EXAFS exhibiting the Fe-O and Fe-Fe bonds.

X-ray absorption spectroscopy (XAS) analysis supports enhanced Fe^{2+}/Fe^{3+} conversion in hybrid electrolytes. **Figure 3a** shows Fe K-edge spectra from the samples obtained from NaOH and hybrid electrolytes, along with Fe_3O_4 (1/3 of Fe^{2+} and 2/3 of Fe^{3+}) and FeOOH (Fe^{3+}) standards. At the fully discharged state (0.2 V vs. Hg/HgO), iron oxides from hybrid electrolytes show high-energy shifted absorption energy at the half-edge step [½μ(E)] compared to the sample in NaOH. From a linear fit of ½μ(E) energy positions between $Fe^{2+/3+}$ and Fe^{3+} spectra from standards in **Figure 3b**, the valences of Fe at fully discharged (0.2V) states were determined to be +2.79 and +2.92 in NaOH and hybrid electrolytes, respectively. The Fourier Transform of EXAFS in R-space (**Figure 3c**) agrees well with energy-space XAS data. FeOOH standard shows higher Fe-O atomic pair intensity at ~1.44 Å and lower Fe-Fe intensity at ~ 2.67 Å than the Fe_3O_4 standard, owing to its higher valence state (namely, more O atoms than Fe atoms surround each Fe atom). Accordingly, discharged iron oxides from hybrid electrolytes show a more robust Fe-O pair and weaker Fe-Fe intensity than that obtained from the NaOH electrolyte, corroborating improved Fe^{2+}/Fe^{3+} conversion.

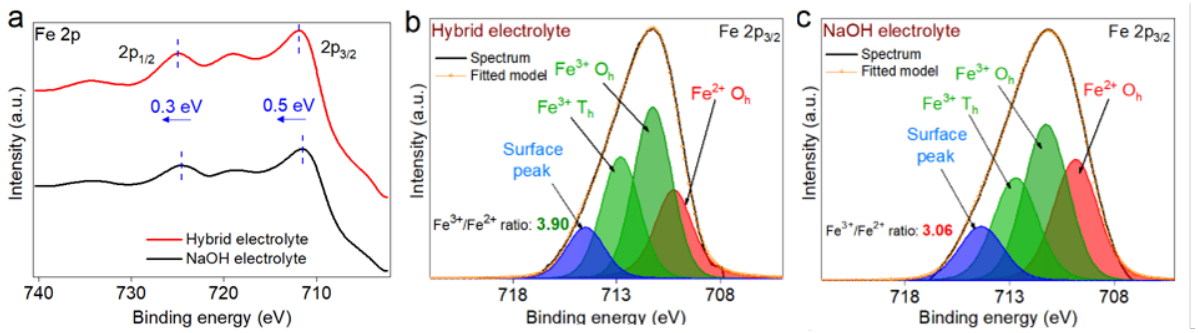

Figure 4. XPS studies of Fe spectra. (a) XPS Fe $2p_{1/2\text{-}3/2}$ spectra of as-made iron oxides. Valence analysis of Fe by multiplet splitting of Fe $2p_{3/2}$ in (b) NaOH and (c) hybrid electrolytes of the discharged materials.

XPS analysis confirms an improved Fe^{2+}/Fe^{3+} conversion in the hybrid electrolyte. **Figure 4a** exhibits the XPS Fe-2p spectra at discharged iron oxides (0.2 V). The Fe $2p_{1/2}$ and $2p_{3/2}$ from hybrid electrolytes shifted to higher binding energy than the NaOH solution, supporting a more oxidized Fe valence state. The quantitative analysis from Fe $2p_{3/2}$ multiplet splitting is shown in **Figures 4b-c** [34, 35], showing a higher Fe^{3+}/Fe^{2+} ratio in the hybrid electrolytes than in NaOH electrolytes (3.90 vs. 3.06) (**Table S1**) [36]. The molar fraction of FeOOH in hybrid electrolytes was calculated to be 65.5%, agreeing with the FeOOH phase fraction of 68% from *operando* XRD. Notably, the charge products of Fe redox, such as $Fe(OH)_2$ or Fe, are susceptible to immediate oxidation once contacting with air during the ex situ characterizations. Thus, the reported XAS and XPS mainly characterize the discharge products.

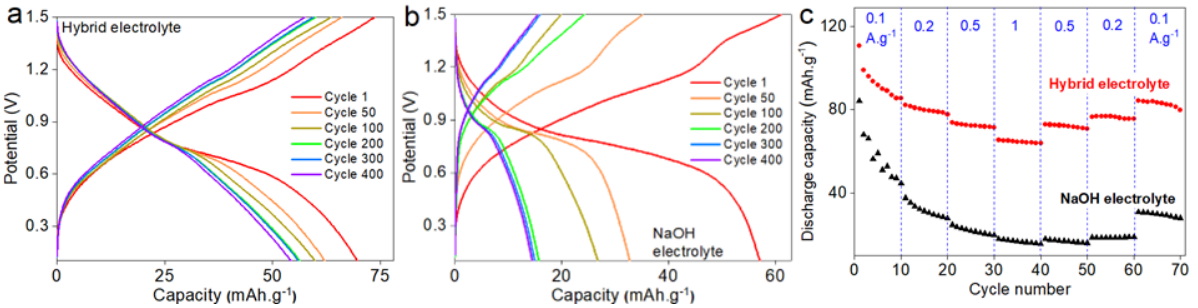

Figure 5. Full cell electrochemical measurements of iron oxides. Charge-discharge profiles in (a) hybrid and (b) NaOH electrolytes at the current density of 0.2 A g^{-1}. (c) Step-rate test comparison between the NaOH electrolyte and hybrid electrolyte depicts better capacity retention in the presence of Na_2SiO_3.

The long-term cycling of $Fe(OH)_2/FeOOH$ redox was studied in a two-electrode full-cell comprised of the iron oxide anode and the overloaded active carbon cathode. When the cathode capacity is much higher due to an overload of active materials, the overall storage capacity of the two-electrode full cells is nearly equivalent to the anode capacity. Iron oxides in hybrid electrolytes show a higher first-cycle discharge capacity (71.2 mAh.g^{-1}) than NaOH electrolyte (57.1 mAh.g^{-1}) and higher capacity retention (76.4% vs. 25.2%) after 400 cycles at

a current density of 0.2 A g^{-1} (**Figures 5a-b).** Consistent with the half-cell measurements, the dQ/dV curves (**Figures S5a-b**) in the hybrid electrolyte depicted an additional redox peak at 0.5 V, compared to that in NaOH electrolyte, attributed to $Fe(OH)_2 \rightarrow FeOOH$ conversion. The rate performance was evaluated using step-rate tests from 0.1 to 1 A g^{-1} (**Figure 5c**). Hybrid electrolyte delivers better capacity retention than NaOH electrolyte (83.9% vs. 62.9%). Full cells operated in hybrid electrolytes demonstrated an excellent coulombic efficiency of 94% after 400 charge/discharge cycles (**Figure S5c**). Notably, the full-cell discharge capacity is lower than that of a three-electrode half-cell measurement. This could be due to the high loading of active materials (1.4 mg versus 40 μg) and low electrolyte volume (0.5 mL versus 25 mL) compared to that in half cells, which might impede the complete redox reaction as seen in half-cells.

2.3. Unraveling impact of Na_2SiO_3 on Fe redox by *operando* XRD

Structural evidence of improved $Fe(OH)_2$/FeOOH conversion in NaOH/Na_2SiO_3 hybrid electrolytes was provided by *operando* XRD studies simultaneously obtained during cyclic voltammetry (CV) cycling between -1.3 V and 0.2 V (vs. Hg/HgO) at a sweep rate of 0.3 mV/s in an *operando* three-electrode half-cell. Unlike the CP tests in **Figure 2**, where 40 μg of materials was drop-casted on the Teflon-shrouded glassy carbon electrode, the *operando* cell used 10 mg of materials deposited on the current collector for the synchrotron XRD analysis. The waterfall plot of *operando* XRD patterns during CV cycling is shown in **Figure S6**.

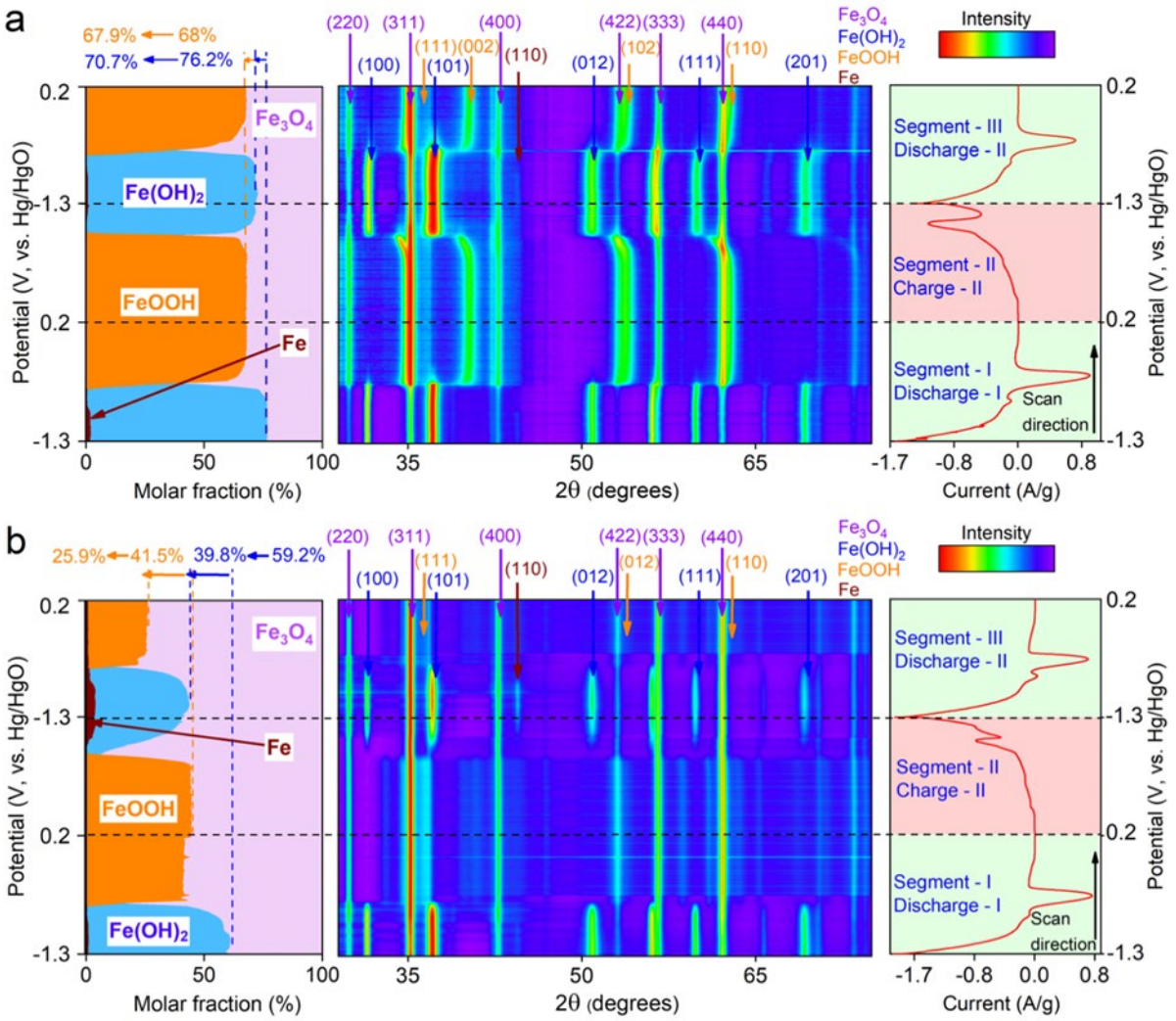

Figure 6. ***Operando*** **XRD studies depict potentiodynamic evolution.** The molar fraction of phases calculated by Rietveld refinement of iron oxides, and contour plots obtained from *operando* XRD measurements conducted in (a) hybrid and (b) NaOH electrolytes simultaneously with CV cycling from -1.3 V to 0.2 V at the sweep rate of 0.3 $mV.s^{-1}$.

Figure 6 shows the contour plots of the XRD pattern of iron oxides in hybrid and NaOH electrolytes, unfolded CV curves, and quantitative Rietveld refinement of potentiodynamic evolution of crystalline phases in molar fractions (based on total Fe atoms). At a fully charged (reduced) state, iron oxides were reduced into $Fe(OH)_2$ (JCPDS 13-0089) with the signature peaks of (001), (011), and (102), following the reactions described in **Equations 1** and **2**. As the potential increased to -0.59 V, ~ 9.6 % of $Fe(OH)_2$ was discharged (oxidized) to Fe_3O_4 (JCPDS 19-0629) with emerging (311), (220), and (400) diffraction peaks, following the inverted **Equation 2**. When the potential continuously increases to -0.54 V, a new set of diffraction peaks appears, exclusively indexed to (111), (002), and (102) of FeOOH (JCPDS 13-87), following the reversed **Equation 1** or reversed **Equation 3**. The FeOOH phase reached a molar fraction of 68% at 0.03 V, much higher than the Fe_3O_4 molar fraction converted from $Fe(OH)_2$ (9.6%), suggesting that $Fe(OH)_2 \rightarrow$FeOOH pathway

accounts for FeOOH formation instead of Fe_3O_4→FeOOH pathway (**Figure S7**). In the consecutive charging (reduction) process, the FeOOH phase disappeared when the potential decreased from 0.2 V to -1.3 V, and $Fe(OH)_2$ formed at the fully charged state. Notably, in the 2nd segment of discharging, nearly identical $Fe(OH)_2$→Fe_3O_4 and $Fe(OH)_2$→FeOOH conversions repeatedly occurred, suggesting good reversibility of observed redox reactions in the hybrid electrolyte.

$$FeOOH + H_2O + e^- \rightarrow Fe(OH)_2 + OH^- \qquad E = -0.582\,V \qquad \textbf{Equation 1}$$

$$Fe_3O_4 + 4H_2O + 2e^- \rightarrow 3Fe(OH)_2 + 2OH^- \qquad E = -0.876\,V \qquad \textbf{Equation 2}$$

$$3\,FeOOH + e^- \rightarrow Fe_3O_4 + H_2O + OH^- \qquad E = 0\,V \qquad \textbf{Equation 3}$$

$$Fe(OH)_2 + 2e^- \rightarrow Fe + 2OH^- \qquad E = -1.017\,V \qquad \textbf{Equation 4}$$

Note: all the electrode potential values are referred to Hg/HgO at pH = 12 [37, 38].

Figure 6b shows the *operando* XRD of iron oxides measured in NaOH solution (without Na_2SiO_3 additives), exhibiting two significant structural differences from hybrid electrolytes: Firstly, $Fe(OH)_2/Fe_3O_4$ became the dominant redox process since the fully discharged materials show 58.5% Fe_3O_4 and only 41.5% FeOOH. Inefficient Fe^{2+}/Fe^{3+} conversion without Na_2SiO_3 additives corroborates the electrochemical tests where iron oxides show poor discharge capacity in NaOH electrolytes. Secondly, $Fe(OH)_2$/FeOOH redox, though it exists in NaOH electrolytes, shows inferior reversibility to that in the hybrid electrolytes. As shown in **Figure S7**, $Fe(OH)_2$ molar fractions significantly decreased in the first two-cycle of CV in NaOH electrolyte (59.2% vs. 39.8%), and so did FeOOH molar fraction (41.5% vs. 25.9%). In stark contrast, hybrid electrolytes offer nearly reversible $Fe(OH)_2$/FeOOH redox, where $Fe(OH)_2$ (76.2% vs. 70.7%) and FeOOH (68% vs. 67.9%) molar fractions remain similar between 1st and 2nd cycles.

2.4. Understanding the Inhibitive Effect of Silicate on HER during Charging by integrating DFT Calculations, Electrochemical Measurements, and XPS

To gain fundamental insights into the effect of Na_2SiO_3 additive on the thermodynamics of HER, we turn to density functional theory (DFT) calculations using the well-established computational hydrogen electrode (CHE) model (**Figure 7**) [39, 40], where the chemical potential of H^+/e^- pairs are defined as half of that of the isolated H_2 molecule. Previous studies have demonstrated that HER under alkaline conditions consists of four elementary steps (**Figure 7a**) [41, 42]:

(i) $* + H_2O \rightarrow H_2O^*$ (water adsorption),

(ii) $H_2O^* \rightarrow H^* + HO^*$ (water dissociation),

(iii) $H^* + HO^* + e^- \rightarrow H^* + OH^-$ (hydroxyl ion desorption),

(iv) $H^* + OH^- \rightarrow \frac{1}{2}H_2 + OH^-$ (hydrogen production)

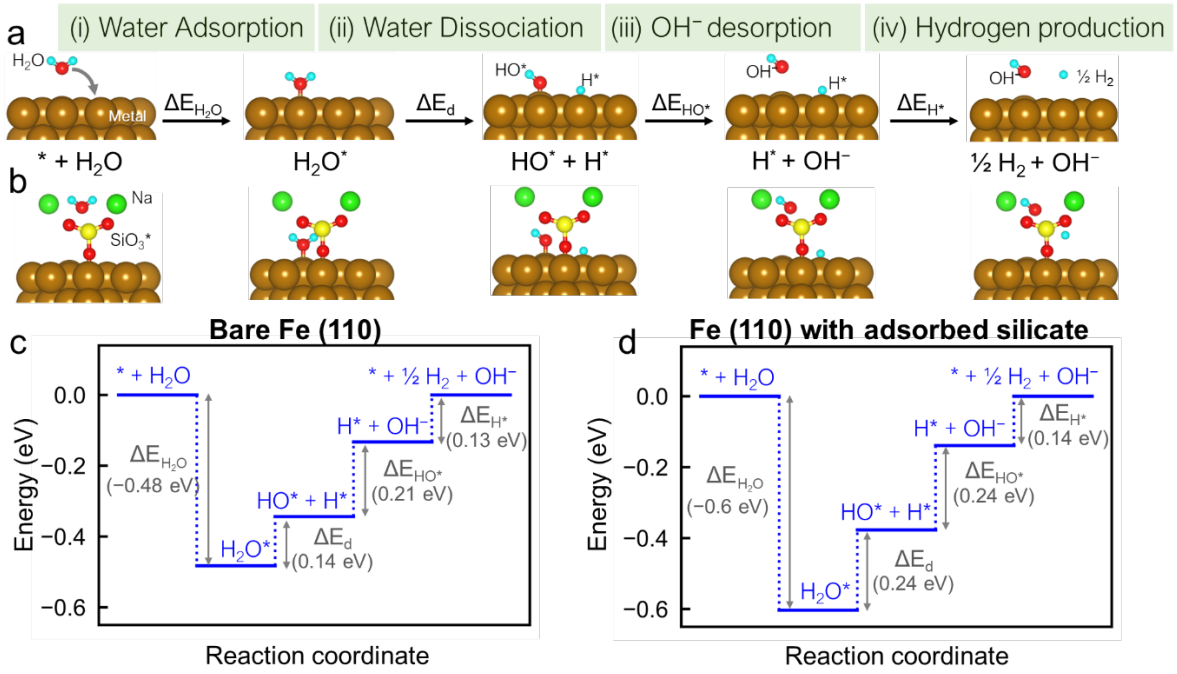

Figure 7. Energetics of hydrogen evolution reaction studied using density functional theory calculations. Schematic illustration of the four elementary steps ((i)-(iv)) involved in HER in an alkaline medium on (a) bare Fe (110) surface, and (b) Fe (110) surface containing an adsorbed silicate. Energy landscape for HER in (a, b) was evaluated using DFT calculations. In panels (c,d) the reaction energies for each of the elementary steps (panel (a)) are indicated.

The reaction energies for each of these steps, ΔE_{H_2O}, ΔE_d, ΔE_{HO*}, and ΔE_{H*} respectively, can be evaluated using total energy DFT calculations (see Methods for details). Note that in the steps (i)-(iv), * refers to the adsorption site on the surface of Fe or $Fe(OH)_2$. First, our DFT-derived energy landscape elucidates that while the adsorption of water on $Fe(OH)_2$ is mildly exothermic (ΔE_{H_2O}~ −0.12 eV), the water dissociation (ΔE_d~1.7 eV) and OH^- desorption (ΔE_{HO*}~2.7 eV) steps are highly endothermic; making HER highly unlikely on $Fe(OH)_2$ for the applied potentials employed in this study. In fact, water dissociation and hydroxyl desorption on $Fe(OH)_2$ are nearly 10 times more endothermic than that on Fe (110) surface (**Figures 7c-d, Figure S8**); which is indicative of a strong thermodynamic preference for HER to occur on Fe rather on $Fe(OH)_2$ surface. This finding is consistent with our CV and *operando* XRD experiments (**Figure 8a** and **Figure S9**), which show clear evidence for concurrent HER current and Fe formation according to **Equation 4**, including (i) emergence of diffraction peaks from (110), (200), and (211) planes of metallic Fe (α-Fe, JCPDS 06-

0696) (~2.7%) at the voltage of -1.17 V during the cathodic scan, and (ii) simultaneous rapid increase in cathodic current with decreasing potential – a tell-tale sign of HER.

Since HER is more likely to occur on Fe than on $Fe(OH)_2$, we employed DFT calculations to elucidate the effects of silicate additives on HER activity of Fe (110) surface, the most stable surface facet of Fe. RMD simulations indicate that the silicate additives exist in the form of SiO_3^{2-}, $H_xSiO_4^{(4-x)-}$, and $Si(OH)_4$ species in the electrolyte, regardless of the concentration of Na_2SiO_3. Importantly, at low silicate concentrations, although $Si(OH)_4$ is the dominant species, significant amounts of $H_xSiO_4^{(4-x)-}$ and SiO_3^{2-} still persist (**Figure S1**). Among these species, we find that the adsorption of $Si(OH)_4$ on Fe(110) is slightly endothermic, with a binding energy of ~0.11 eV (Figure S10), and is, therefore, unlikely to impact HER activity. However, all the other silicate species adsorb more strongly on Fe(110) relative to water, showing nearly 6 – 8 times more negative adsorption energy ($HSiO_4^{3-}$: –2.74 eV; $H_2SiO_4^{2-}$: –3.22 eV; $H_3SiO_4^{-}$: –3.31 eV; and SiO_3^{2-}: –4 eV) than water (–0.48 eV). Such strong binding of the SiO_3^{2-} / $H_xSiO_4^{(4-x)-}$ species on Fe(110) is facilitated by a higher charge transfer during their adsorption, as compared to water. For instance, adsorption of isolated SiO_3^{2-} and water on Fe(110) results in charge transfer of ~0.22*e*, and ~0.19*e*, respectively (**Figure S11**); this also manifests in a shorter bond between O of SiO_3^{2-} and Fe (1.74 Å) than for water (Fe-O_w: 2.08 Å) (**Figure S11**). Evidently, the presence of Na_2SiO_3 additive in the hybrid electrolyte would thwart water binding on Fe by limiting access to adsorption sites. Nevertheless, at a low Na_2SiO_3 concentration (e.g., 150 ppm, used in this study), a significant fraction of sites on Fe(110) would still be available for adsorbing water.

We evaluated the impact of the adsorbed SiO_3^{2-} / $H_xSiO_4^{(4-x)-}$ species on the energetics of the elementary steps involved in HER on Fe(110). Interestingly, we find that the presence of SiO_3^{2-} (the most strongly binding species) in the vicinity of adsorbing water on Fe (110) facilitates a stronger binding of water (ΔE_{H_2O}~ –0.6 eV) as compared to that on bare Fe(110) (ΔE_{H_2O}~ –0.48 eV) due to strong HB interactions between the adsorbed species, *i.e.*, SiO_3^{2-} and H_2O (**Figures 7b-d**). Importantly, these HB interactions also make water dissociation (ΔE_d~0.24 eV) and OH^- desorption (ΔE_{HO*}~ 0.24 eV) significantly more uphill, than that on bare Fe (110) (Figures 7c,d). Similarly, the presence of a proximal $H_2SiO_4^{2-}$ on Fe(110) surface enhances binding of incoming water (ΔE_{H_2O}~ –0.82 eV); the HB interactions between adsorbed $H_2SiO_4^{2-}$ and water renders both water dissociation (ΔE_d~0.37 eV), and hydroxyl desorption (ΔE_{HO*}~ 3.58 eV) steps highly endothermic (**Figure S12**). The other $H_xSiO_4^{(4-x)-}$ species (i.e., $HSiO_4^{3-}$, $H_3SiO_4^{-}$) do not show sufficient HB interactions with water to impact

water adsorption and dissociation steps. Nevertheless, the HB interactions between adsorbed HO*, H*, and $HSiO_4^{3-}$/$H_3SiO_4^-$ species make the hydroxyl adsorption steps extremely uphill (ΔE_{HO*} values for $HSiO_4^{3-}$: 3.75 eV; $H_3SiO_4^-$: 3.49 eV) as shown by **Figure S13** and **Figure S14**. Clearly, the rate-limiting elementary step (i.e., the step with the most positive reaction energy) for HER in the presence of adsorbed SiO_3^{2-} / $H_xSiO_4^{(4-x)-}$ species is significantly more endothermic than that on bare Fe(110). This, in turn, increases the necessary overpotential to drive HER on silicate-covered Fe(110); demonstrating that silicate additives in the hybrid electrolyte would mitigate HER. Indeed, our electrochemical experiments suggest that the hybrid electrolyte requires a lower reduction potential (namely, a larger activation barrier) for HER than the NaOH electrolyte ($\Delta V = 0.116V$), as illustrated in **Figure 8a**, which corroborates that the Na_2SiO_3 additives suppress parasitic HER. A lower TAFEL slope for HER in NaOH electrolyte than hybrid electrolyte (142.6 mV.dec^{-1} vs. 296.1 mV.dec^{-1}) further indicated a faster HER kinetics without the Na_2SiO_3 additive (**Figure S15**).

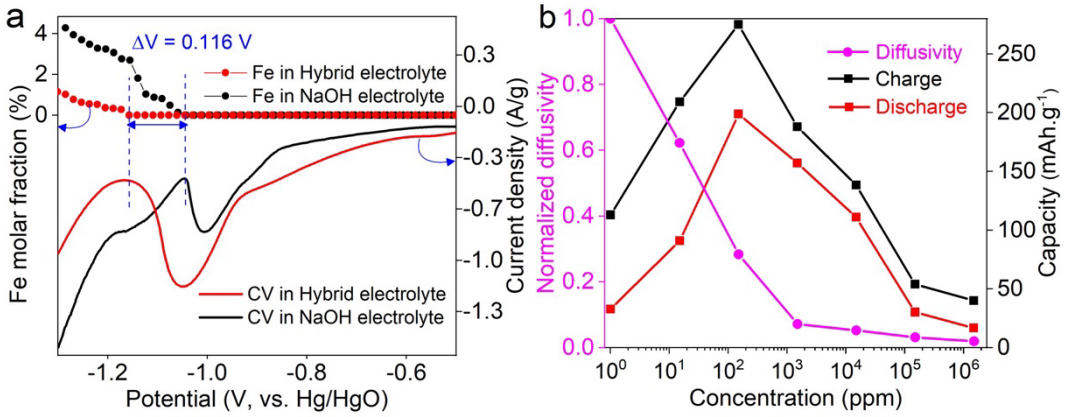

Figure 8. **Influences of silicate on iron oxide during charge and discharge processes**. (a) The current density from CV measurement and metallic Fe molar fractions from simultaneous operando XRD in hybrid and NaOH electrolytes. (b) Normalized diffusivities and discharge capacities of iron oxides in 0.01 M NaOH with various Na_2SiO_3 concentrations ranging from 0 ppm to 1,500,000 ppm.

The strong interaction between iron oxide and SiO_3^{2-} anions was supported experimentally by XPS measurements. Si-2p (**Figure 9a**) and Si-2s (**Figure 9b**) spectra of fully discharged iron oxides (0.2 V) in hybrid electrolytes (0.01 M NaOH/1500 ppm Na_2SiO_3) shifted to a lower binding energy than the Na_2SiO_3 standard, suggesting a decreased electron density of Si site upon Na_2SiO_3/iron oxide interaction. Similar trends can also be found in Si-2p and Si-2s spectra from iron oxide materials at different voltages (-0.5 V and 0.2 V) using different silicate concentrations (500 ppm and 1500 ppm) (**Figures S16a-d**). **Figure 9c** and **Figure S16e-f** present the O 1s spectra of iron oxides cycled in the hybrid and NaOH electrolytes, where two subpeaks at 531 eV and 534 eV are attributed to the Fe-O-Fe or Fe-O-OH oxygen atoms (lattice oxygen) and oxygen atoms from adsorbed hydroxyl ions,

respectively. Iron oxides in hybrid electrolytes had a weaker interaction with hydroxyl ions, indicating that the strong silicate-iron oxide interaction alleviates the hydroxyl ions (from water) absorption, which agrees well with our DFT calculations (**Figure S17**). This also agrees with previous experimental studies on sodium iron silicate glasses, showing adsorbed oxygenous species decreased with concentrated silicate due to enhanced Si-O-Fe bonding [43].

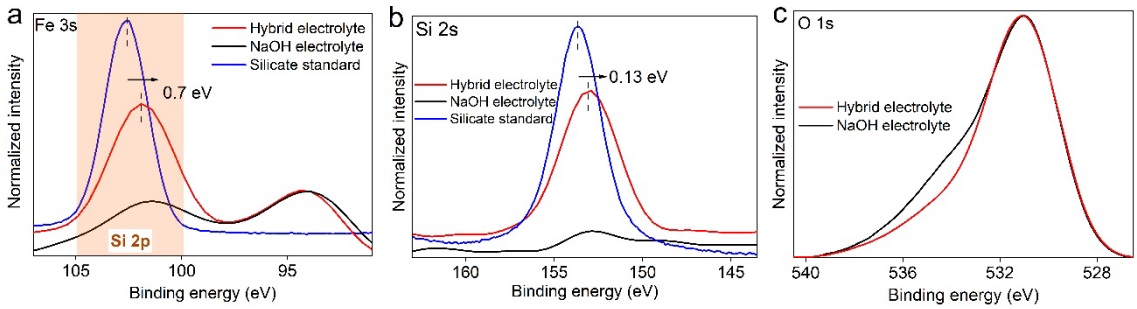

Figure 9. XPS studies of Si and O spectra of discharged materials. (a) Si 2p and Fe 3s and (b) Si 2s spectra of fully discharged iron oxides (0.2 V) in NaOH and hybrid electrolytes compared with the Na_2SiO_3 standard, indicating the Fe-O-Si interaction through the negative binding energy shift. (c) O 1s spectra of fully discharged iron oxides (0.2V) in both electrolytes.

DFT calculations indicate that SiO_3^{2-}/ $H_xSiO_4^{(4-x)-}$ species present in the hybrid electrolyte exhibit a strong thermodynamic preference to adsorb on the surface of $Fe(OH)_2$, as compared to hydroxyl ions (**Figure S17**). This is evidenced by the significantly more exothermic binding energies for SiO_3^{2-} (~ –3.09 eV), $H_2SiO_4^{2-}$ (~ –1.68 eV), and $H_3SiO_4^-$ (~ –1.59 eV) on $Fe(OH)_2$ (001) than that for hydroxyl ions (~ –1.29 eV); the binding energy for $HSiO_4^-$ (~ –1.24 eV) is on-par with that for hydroxyl ions. Such a strong preference for adsorption of SiO_3^{2-}/ $H_xSiO_4^{(4-x)-}$ species over OH^- shields the interaction between $Fe(OH)_2$ and hydroxyl ions by limiting the adsorption sites. This, in turn, would severely impair the kinetics of $Fe(OH)_2$ conversion reactions, especially those that require multiple OH^- ions, such as $Fe(OH)_2$ to Fe_3O_4 (**Equation 2**).

Figure 8b shows the influence of Na_2SiO_3 concentrations on the diffusivity, charge, and discharge capacities. In the hybrid electrolytes with various Na_2SiO_3 concentrations ranging from 0 ppm to 1,500,000 ppm (or 1.5 M), the diffusion coefficient of hydroxyl ions, measured using the current pulse relaxation method [44], decreased 51.6 times from 0 ppm to 1.5 M; with iron oxides in 150 ppm Na_2SiO_3 delivering the highest discharge and charge capacities. When more concentrated Na_2SiO_3 was used, strongly blocking from water and hydroxyl made iron oxides inactive toward redox reaction. The blocking effect of silicate on the ion transport is also qualitatively supported by RMD calculation (**Figure 1**), showing that

including Na^+ ions in the solvation shell of water with increasing Na_2SiO_3 concentrations abates the diffusivity of water molecules and hydroxyl ions. Notably, our previous results suggested that the $Fe(OH)_2$/FeOOH conversion was favored when water transport was limited in a weak alkaline solution, while $Fe(OH)_2/Fe_3O_4$ conversion was favored in a strong alkaline solution where water transport was fast. Thus, the inhibitive effects of silicate on water transport and, thus, the Fe_3O_4 formation reported in this study are congruent with previous results. We acknowledge that while silicate decreased water activity and stabilized the iron oxide surface necessary for selective $Fe(OH)_2$ → FeOOH conversion, over-concentrated Na_2SiO_3 inevitably shields the iron oxide from charge carriers and blocks the redox activities (**Figure 8b** and **Figure S14**).

3. Discussion

The Fe^0/Fe^{3+} three-electron transfer is attractive in Fe alkaline batteries. However, our studies question the overall benefits of Fe^0/Fe^{3+} redox for two reasons: (i) the formation of metallic Fe on charging catalyzed the HER, impairing the coulombic efficiency and significantly impeding the complete reduction of Fe_3O_4 or FeOOH to $Fe(OH)_2$; (ii) the low $Fe(OH)_2$ conversion on charging, in turn, resulted in a low discharge capacity since FeOOH formation is through $Fe(OH)_2$→FeOOH pathway instead of Fe_3O_4→FeOOH pathway. Our work demonstrates silicate additives could alleviate above concerns in Fe alkaline redox chemistries, and we found out strong interaction between silicate and iron oxide has three-pronged effects on improving the $Fe(OH)_2$ formation on charging, FeOOH formation on discharging, and overall Fe^{2+}/Fe^{3+} redox stability.

Firstly, silicate/iron oxide interaction benefits a more complete charging of iron oxides. **Figure 8a and Figure S7** show that once Fe forms (even with a molar fraction as low as 1.0 %), the overall charging current is mainly attributed to HER, which impairs the coulombic efficiency and impedes the continuous reduction of remaining iron oxides to $Fe(OH)_2$. The Na_2SiO_3 immobilizes water by rearranging the HB network in the electrolytes and shields iron oxide from water, resulting in a high overpotential for Fe formation. Mitigating Fe formation allows an improved Fe_3O_4→$Fe(OH)_2$ conversion, supported by *operando* XRD showing higher $Fe(OH)_2$ fractions in hybrid electrolytes (76.2% and 70.7% in 1st and 3rd segments) than NaOH electrolyte (59.2% and 39.8% in 1st and 3rd segments), as shown in **Table 1**. In addition, DFT calculations, electrochemical measurements, and XPS indicate that the strong iron/silicate interactions also suppress HER (**Figures 4,7,8**).

Secondly, strong silicate/iron oxide interaction benefits the discharging performance. Without Na_2SiO_3, incomplete reduction of $Fe_3O_4 \rightarrow Fe(OH)_2$ on charging takes a toll on the discharge process since FeOOH formation follows the $Fe(OH)_2 \rightarrow$FeOOH pathway instead of the $Fe_3O_4 \rightarrow$FeOOH pathway. In hybrid electrolytes, a high fraction of $Fe(OH)_2$ formation (76.2%) on charging benefits the high fraction of FeOOH formation (68%) on the consecutive discharging cycle, along with a much-improved discharge capacity (**Table 1**).

Thirdly, silicate/iron oxide interaction stabilizes Fe^{2+}/Fe^{3+} redox, reflected by the phase ratio retention in the first two cycles of *operando* XRD measurements (**Figure 6** and **Figure S6**). Specifically, retention of $Fe(OH)_2$ (and FeOOH) molar fractions in NaOH electrolyte at charged (and discharged) states are 67% (and 62%). In stark contrast, hybrid electrolytes offer much-improved phase ratio retention for $Fe(OH)_2$ (93%) and FeOOH (100%).

4. Conclusion

In summary, we demonstrated that silicate additives, a new type of MCA effective in ppm-level concentrations, increased hydrogen bonding strength and decreased water transport in the electrolyte, strongly interacted with the iron oxide surface, and thus mitigated the H_2 and Fe_3O_4 formation on charge and discharge, respectively. Such interactions alleviate metallic Fe formation on charging and deleterious HER and allow the more complete formation of $Fe(OH)_2$ (up to 76.2% of $Fe^{3+} \rightarrow Fe^{2+}$ conversion), disclosed by multiple physical and electrochemical characterization techniques. The high $Fe^{3+} \rightarrow Fe^{2+}$ conversion on charging, in turn, benefits the discharge process by favoring $Fe(OH)_2 \rightarrow$ FeOOH conversion. With the Na_2SiO_3 additive, the storage capacity of the iron oxide anode was six times higher than that in a conventional NaOH electrolyte. The $Fe(OH)_2$ anode showed excellent cycle stability in full cells. Our work shed light on utilizing silicate to expedite the development of a low-cost and safe aqueous energy storage system when combined with other materials and electrolyte advances.

5. Materials and Methods

Material synthesis: The following chemicals were used as purchased for the synthesis: Ferrous sulfate heptahydrate ($FeSO_4.7H_2O$, 2.085 g) (Alfa Aesar) and Ferric sulfate ($Fe_2(SO_4)_3.xH_2O$, 0.66 g) were dissolved in 50 mL of degassed deionized (DI) water at 350 rpm till it was a clear brown solution. 0.6 g of NaOH (Alfa Aesar) dissolved in 50 mL of degassed DI water was added to the mixture of iron salts. The solution was stirred for 24 hours at 850 rpm with Argon flow overhead throughout the synthesis. The obtained product

was centrifuged, washed, dried overnight passing Argon gas, grounded with agate mortar and pestle, and stored in an inert gas-filled desiccator for material and electrochemical characterizations.

Material characterization: SEM image was obtained from Tescan Lyra3 GMU FIB-SEM at the University Instrumentation Center (UIC), University of New Hampshire. The powder sample was sprinkled on the top of the carbon-painted stub and sputtered with 12 nm of Au-Pd alloy before the analysis for better imaging.

Half-cell electrochemical studies: CP measurements were conducted in CH Instruments 660D/E electrochemical workstation. A three-electrode half-cell system was designed using a glassy carbon rotating-disk working electrode coated with the active material, a counter platinum wire electrode, and a mercury/mercury oxide reference electrode filled with 1M NaOH solution. The ink was prepared by mixing the 7:3 ratio of the synthesized sample and carbon black with a concentration of 1 mg/mL. Then, 40 µg of active material was loaded on the working electrode and 20 µL of 1% Nafion 117 (Sigma Aldrich) was coated and vacuum dried on the top of the electrode material as a binder to prevent material dissolution into the electrolyte.

A 25 mL plastic flask containing 0.01 M NaOH and x parts per million (ppm) of sodium silicate (Sigma Aldrich) was used to conduct the C.P. measurements, and the electrolyte was bubbled with Argon gas before the half-cell measurements to degas the dissolved oxygen. The CP data was collected within the potential window of -1.05 V to 0.2 V (vs. Hg/HgO) for 7 cycles with an applied current density of 0.1 A/g. Since the first cycle is dedicated to the activation of the electrode material, data from the second cycle is taken into consideration. The diffusivity measurements were conducted using the same three-electrode system as described above. After attaining open circuit potential (OCP) following the first charging cycle, a short negative current pulse of 0.25 A/g is applied for 25 seconds to charge the working electrode. It is then allowed for relaxation, and the rate of decay of the resulting transient voltage is collected for 800 s.

Full-cell cycling: Asymmetric two-electrode full cells were assembled in ECC-Aqu electrochemical cells (EL-Cell) for CP measurements. The ink for the anode mixture was prepared by adding 70% of synthesized iron oxides, 30% carbon black, 8.68 µL of 10% diluted Styrene-Butadiene Rubber (SBR) (MTI) in 0.8 mL of EtOH and 0.2 mL of DI H_2O. 200 mg Carbon black Vulcan XC-72R, and 86.84 µL S.B.R. was mixed in 16 mL of EtOH for the cathode. Toray carbon papers (40% Teflon) were cut into 18 mm diameter discs with 0.4

mm thickness. 20 mg of the cathodic mixture and 2 mg of the anodic mixture were drop-casted on the carbon paper discs and dried in ambient conditions. Five pieces of Whatman filter paper 1 (pore size 11 μm) were also cut in the same diameter and used as separators. All the full-cell CP measurements were carried out at room temperature at 0.2 A g^{-1} at the potential range of 0.1 V to 1.5 V for 400 cycles using the Arbin BT-G battery cycler.

X-ray scattering measurements: *Operando* X-ray scattering measurements were done at the 28-ID-1 beamline at the National Synchrotron Light Source – II in Brookhaven National Laboratory with a synchrotron beam wavelength of $\lambda = 0.1665$ Å. The working electrodes were 10 mg of the mixture (7:3 ratio of iron oxides: carbon black) was drop-casted over the 5% Teflon-coated Toray carbon paper (Fuel Cell Earth). Then, cyclic voltammetry was conducted from 0.2 V to -1.3 V (vs. Hg/HgO) by assembling a homemade electrochemical cell. Simultaneously, the XRD images were captured in a 2D area detector every minute during the cycling.

X-ray absorption spectroscopy: XAS measurements were done at beamline 6-BM Beamline for Materials Measurement at the National Synchrotron Light Source-II, Brookhaven National Laboratory. The samples with 2 mg loading were cycled with CV in corresponding electrolytes and held at the oxidation potential of 0.2 V (vs. Hg/HgO) for 15 minutes and dried under a vacuum before placing them for data collection. The XAS measurements were carried out in transmission mode at the Fe K-edge (7112 eV). Fe metal foil and iron oxide powders (Fe_3O_4, and FeOOH) were used as references for X-ray energy calibration and data alignment. The imaginary part of the complex $\chi(R)$ was calculated from EXAFS by taking the Fourier Transform of weighted $k^2\ \chi(k)$. Athena software from the Demeter package was used to perform XAS data processing and analysis.

X-ray photoelectron spectroscopy: XPS measurements were carried out in Kratos Axis Supra XPS using Al Kα monochromatic source at the UIC, University of New Hampshire. The samples after discharged with CP at various potentials in various Na_2SiO_3 concentrations, the electrodes were fixed on the sample holder using copper tape and studied in a vacuum of the order of 10^{-8} Torr. Obtained spectra were processed using the CasaXPS software package. All the Fe-2p peaks were calibrated using the adventitious carbon peak at the binding energy of 284.8 eV of the C 1s line.

Reactive molecular dynamics simulations: All the reactive molecular dynamics (RMD) simulations were performed using the well-established open-source simulation package (LAMMPS) [45-47]. To model the electrolyte, we employed a computational supercell (120 Å

×120 Å × 120 Å) containing 15,000 water molecules and 3 NaOH molecules, corresponding to 0.01 M aqueous solution of NaOH. Periodic boundary conditions were employed in all directions. We added the required number of SiO_3 ions along with Na^+ counter ions at random locations within the computational supercell to build initial configurations at desired Na_2SiO_3 concentrations (that range from 0 M to 4.9 M). All atomic interactions in the system were described using a reactive force field (ReaxFF), with parameters developed by Hahn *et al.* for $NaSiO_x$/water system [48]. This set of ReaxFF parameters has been found to accurately describe the solvation behavior of Na^+ and SiO_3^{2-} ions with water, ionic transport, dissociation behavior of NaOH in water, as well as reactivity and leaching of silicate glasses in an aqueous environment [48, 49].

First, we equilibrated all the initial configurations at various Na_2SiO_3 concentrations within an isobaric-isothermal ensemble (*NPT*) under ambient conditions for 0.5 ns. The equilibrated density at the end of *NPT* runs was 1 – 1.15 g/cc, in excellent agreement with our experiments. Note, the density increases slightly with an increase in Na_2SiO_3 concentration (0 M: 0 g/ml; 4.9 M: 1.15 g/ml). Thereafter, we performed production runs within the canonical ensemble (*NVT*) for 1.5 ns under ambient conditions.

The diffusivity of water molecules was calculated from the time evolved mean square displacements using the Einstein relationship, averaged over the last 1ns of the RMD. trajectories. To determine the average solvation energy E_{sol} at a given Na_2SiO_3 concentration, we first extracted solvation clusters around all water molecules (i.e. configuration of first solvation shells along with their atomic charges) in 100 representative snapshots from the last 1 ns of RMD trajectory. Next, the interaction energy between water and the molecules within each solvation cluster (called solvation energy) was evaluated using static calculations in the framework of ReaxFF to obtain the average E_{sol}. Hydrogen bond (HB) analysis was performed by using a well-established configurational criterion, wherein two water molecules are considered to be connected by H.B. only if (a) the oxygen atoms of the water molecules lie within 3.5 Å of each other, and (b) the O—H … O angle is less than 30° [50]. A binary function $h(t)$ is employed to determine whether a given pair of water molecules are connected via H.B. at time t. The value of h is unity for hydrogen-bonded pairs and is zero otherwise. The dynamics of the H.B. network are characterized by the correlation function: $C(t) = \langle h(0)h(t)\rangle / \langle h(0)h(0)\rangle$, where the angle brackets denote the average over all distinct pairs of water molecules and initial timeframes. [50, 30, 51].

Density functional theory calculations: All the first principles calculations were performed within the framework of Hubbard-corrected density functional theory (DFT+*U*) using the projected augmented plane wave method as implemented in Vienna Ab initio Simulation Package (VASP) [52, 53]. The exchange correlations were described using the Perdew-Burke-Ernzerhof (P.B.E.) functionals within the generalized gradient approximation algorithm using the pseudopotentials provided by VASP: Na_pv (valence: $2p^6\ 3s^1$), Fe_pv ($3p^6\ 3d^6\ 4s^2$), Si ($3s^2\ 3p^2$), H (valence: $1s^1$), O (valence: $2s^2\ 2p^4$) [54]. Hubbard correction (U = 5.3 eV and J = 0.0 eV) was employed to treat electron localization on Fe atoms using a rotationally-invariant form of DFT + *U* formulated by Liechtenstein *et al* [55]. The computational supercell consisted of a (001) slab of $Fe(OH)_2$ with 2 × 4 × 1 unit cells, and oriented such that the surface normal points along the crystallographic [001] direction. Periodic boundary conditions are employed along all directions; a vacuum of 23 Å is employed along the surface normal to avoid spurious interactions between periodic images. The plane wave energy cutoff was set at 520 eV and a 2 × 1 × 1 Γ-centered Monkhorst-Pack *k*-grid to sample the Brillouin zone. Gaussian smearing with a width of 0.05 eV was employed. All the atomic coordinates were optimized using a conjugate gradient method until the atomic forces are less than 0.005 eV/Å. The long-range van der Waals interactions were accounted using the DFT-D3 method of Grimme with a zero-damping function implemented in VASP [56]. To determine the adsorption energies of $O.H.^-$ and SiO_3^{2-}, we first relaxed the configuration of the pristine slab. Thereafter, we introduced $O.H.^-$/ SiO_3^{2-} near the surface of (001) $Fe(OH)_2$ slab, while Na^+ ions were added far away from the surface to achieve charge balance. Several adsorption configurations were investigated to identify the most energetically stable one (i.e., the most negative binding energy). For any given adsorption energy configuration, the binding energy of the ion is evaluated as $E_b = E_{ad} - E_{ion} - E_{slab}$, where E_{ad} is the total energy of the slab with the adsorbed ion, while E_{ion} and E_{slab} are the energy of the isolated ion, and pristine slab, respectively.

Supporting Information

Supporting Information is available from the Wiley Online Library or from the author.

Acknowledgments

This research used 28-ID-1 and 6-BM beamlines of the National Synchrotron Light Source II, a US DOE Office of Science User Facility operated for the D.O.E. Office of Science by Brookhaven National Laboratory under Contract No. DE-SC0012704. This research used resources of the National Energy Research Scientific Computing Center, a D.O.E. Office of

Science User Facility supported by the Office of Science of the U.S. Department of Energy under Contract No. DE-AC02-05CH11231 (RP, BN). We thank Dr. Bruce Ravel for assisting with the XAS experiments at Beamline 6-BM.

Funding

National Science Foundation Award Number 2236704 (SNJ, XT)

National Science Foundation Award Number 2216048 (RP, BN)

Author contributions

Conceptualization and experiment design: XT

Material synthesis, characterizations, and electrochemical experiments: SNJ

Operando X-ray measurements: FG, SNJ, MA, GK, DO

X-ray analysis: SNJ

Atomic-scale simulations – design and guidance: BN

Atomic-scale simulations: RTP

Writing – original draft: XT, SNJ

Writing – contributions: RTP, BN

Results discussion and comments: SNJ, FG, RTP, MA, GK, DO, BN, XT

Project supervision: XT

Competing interests

Authors declare that they have no competing interests.

Data and materials availability

All data are available in the main text or the supplementary materials.

Received: ((will be filled in by the editorial staff))

Revised: ((will be filled in by the editorial staff))

Published online: ((will be filled in by the editorial staff))

References

The authors report that the silicate-added hybrid electrolyte strongly interacts with iron oxide during charge to control the competing hydrogen evolution, thus improving conversion. In discharge, one electron transfer to $Fe(OH)_2$/FeOOH conversion is achieved by mitigating electrochemically inactive Fe_3O_4 formation. Such innovation provides a path for designing effective aqueous electrolytes for enabling sustainable energy storage applications by repurposing iron rust.

Sathya Narayanan Jagadeesan, Fenghua Guo, Ranga Teja Pidathala, A.M. Milinda Abeykoon, Gihan Kwon, Daniel Olds, Badri Narayanan, and Xiaowei Teng**

Unlocking High Capacity and Reversible Alkaline Iron Redox using Silicate-Sodium Hydroxide Hybrid Electrolytes

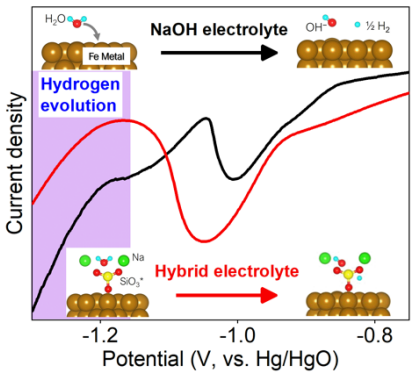

(1) M. S. Whittingham. Lithium batteries and cathode materials. *Chem. Rev.* **104** (10), 4271-4301 (2004).
(2) B. Dunn; H. Kamath; J. M. Tarascon. Electrical Energy Storage for the Grid: A Battery of Choices. *Science* **334** (6058), 928-935 (2011).
(3) K. Mongird; V. Viswanathan; J. Alam; C. Vartanian; V. Sprenkle; R. Baxter. *2020 Grid Energy Storage Technology Cost and Performance Assessment*; DOE/PA-0204; Pacific Northwest National Laboratory & Mustang Prairie Energy, US DOE, 2020.
(4) F. Cheng; J. Chen. Metal–air batteries: from oxygen reduction electrochemistry to cathode catalysts. *Chem. Soc. Rev.* **41** (6), 2172-2192 (2012).
(5) K. F. Blurton; A. F. Sammells. Metal/air batteries: Their status and potential — a review. *J. Power Sources* **4** (4), 263-279 (1979).
(6) X. Hong; J. Mei; L. Wen; Y. Tong; A. J. Vasileff; L. Wang; J. Liang; Z. Sun; S. X. Dou. Nonlithium Metal–Sulfur Batteries: Steps Toward a Leap. *Adv. Mater.* **31** (5), 1802822 (2019).
(7) X. Yu; A. Manthiram. A Progress Report on Metal–Sulfur Batteries. *Adv. Funct. Mater.* **30** (39), 2004084 (2020).
(8) X. Wu; A. Markir; Y. Xu; C. Zhang; D. P. Leonard; W. Shin; X. Ji. A Rechargeable Battery with an Iron Metal Anode. *Adv. Funct. Mater.* **29** (20), 1900911 (2019).

(9) J. Islam; R. Anwar; M. Shareef; H. M. Zabed; J. N. Sahu; X. Qi; M. U. Khandaker; A. Ragauskas; I. Boukhris; M. R. Rahman; et al. Rechargeable metal-metal alkaline batteries: Recent advances, current issues and future research strategies. *J. Power Sources* **563**, 232777 (2023).
(10) W. Shang; W. Yu; Y. Liu; R. Li; Y. Dai; C. Cheng; P. Tan; M. Ni. Rechargeable alkaline zinc batteries: Progress and challenges. *Energy Storage Mater.* **31**, 44-57 (2020).
(11) R. D. McKerracher; C. P. de Leon; R. G. A. Wills; A. A. Shah; F. C. Walsh. A Review of the Iron-Air Secondary Battery for Energy Storage. *Chempluschem* **80** (2), 323-+ (2015).
(12) C. Chakkaravarthy; P. Periasamy; S. Jegannathan; K. I. Vasu. The nickel/iron battery. *J. Power Sources* **35** (1), 21-35 (1991).
(13) A. K. Manohar; C. Yang; S. R. Narayanan. The Role of Sulfide Additives in Achieving Long Cycle Life Rechargeable Iron Electrodes in Alkaline Batteries. *J. Electrochem. Soc.* **162** (9), A1864-A1872 (2015).
(14) H. Kitamura; L. Zhao; B. T. Hang; S. Okada; J.-i. Yamaki. Effect of Charge Current Density on Electrochemical Performance of Fe/C Electrodes in Alkaline Solutions. *J. Electrochem. Soc.* **159** (6), A720-A724 (2012).
(15) F. Guo; S. N. Jagadeesan; R. T. Pidathala; S. Kim; X. Shan; N. A. Deskins; A. M. M. Abeykoon; G. Kwon; D. Olds; B. Narayanan; et al. Revitalizing Iron Redox by Anion-Insertion-Assisted Ferro- and Ferri-Hydroxides Conversion at Low Alkalinity. *J. Am. Chem. Soc.* **144** (27), 11938-11942 (2022).
(16) S. N. Jagadeesan; G. D. Barbosa; F. Guo; L. Zhang; A. M. M. Abeykoon; G. Kwon; D. Olds; C. H. Turner; X. Teng. Chloride Insertion Enhances the Electrochemical Oxidation of Iron Hydroxide Double-Layer Hydroxide into Oxyhydroxide in Alkaline Iron Batteries. *Chem. Mater.* **35** (16), 6517-6526 (2023).
(17) D. Aurbach; B. Markovsky; G. Salitra; E. Markevich; Y. Talyossef; M. Koltypin; L. Nazar; B. Ellis; D. Kovacheva. Review on electrode–electrolyte solution interactions, related to cathode materials for Li-ion batteries. *J. Power Sources* **165** (2), 491-499 (2007).
(18) C. Yan; R. Xu; Y. Xiao; J.-F. Ding; L. Xu; B.-Q. Li; J.-Q. Huang. Toward Critical Electrode/Electrolyte Interfaces in Rechargeable Batteries. *Adv. Funct. Mater.* **30** (23), 1909887 (2020).
(19) Z. Yang; J. He; W.-H. Lai; J. Peng; X.-H. Liu; X.-X. He; X.-F. Guo; L. Li; Y. Qiao; J.-M. Ma; et al. Fire-Retardant, Stable-Cycling and High-Safety Sodium Ion Battery. *Angew. Chem. Int. Ed.* **60** (52), 27086-27094 (2021).
(20) L. M. Suo; O. Borodin; W. Sun; X. L. Fan; C. Y. Yang; F. Wang; T. Gao; Z. H. Ma; M. Schroeder; A. von Cresce; et al. Advanced High-Voltage Aqueous Lithium-Ion Battery Enabled by "Water-in-Bisalt" Electrolyte. *Angew. Chem.-Int. Edit.* **55** (25), 7136-7141 (2016).
(21) L. M. Suo; O. Borodin; Y. S. Wang; X. H. Rong; W. Sun; X. L. Fan; S. Y. Xu; M. A. Schroeder; A. V. Cresce; F. Wang; et al. "Water-in-Salt" Electrolyte Makes Aqueous Sodium-Ion Battery Safe, Green, and Long-Lasting. *Adv. Energy Mater.* **7** (21), 10 (2017).
(22) J. Xie; Z. Liang; Y.-C. Lu. Molecular crowding electrolytes for high-voltage aqueous batteries. *Nat. Mater.* **19** (9), 1006-1011 (2020).
(23) D. E. Ciurduc; C. d. l. Cruz; N. Patil; A. Mavrandonakis; R. Marcilla. Molecular crowding bi-salt electrolyte for aqueous zinc hybrid batteries. *Energy Storage Mater.* **53**, 532-543 (2022).
(24) J. Liu; C. Yang; X. Chi; B. Wen; W. Wang; Y. Liu. Water/Sulfolane Hybrid Electrolyte Achieves Ultralow-Temperature Operation for High-Voltage Aqueous Lithium-Ion Batteries. *Adv. Funct. Mater.* **32** (1), 2106811 (2022).
(25) Y. Wang; T. Wang; S. Bu; J. Zhu; Y. Wang; R. Zhang; H. Hong; W. Zhang; J. Fan; C. Zhi. Sulfolane-containing aqueous electrolyte solutions for producing efficient ampere-hour-level zinc metal battery pouch cells. *Nat. Commun.* **14** (1), 1828 (2023).

(26) C. Li; R. Kingsbury; A. S. Thind; A. Shyamsunder; T. T. Fister; R. F. Klie; K. A. Persson; L. F. Nazar. Enabling selective zinc-ion intercalation by a eutectic electrolyte for practical anodeless zinc batteries. *Nat. Commun.* **14** (1), 3067 (2023).
(27) P. Albertus; J. S. Manser; S. Litzelman. Long-Duration Electricity Storage Applications, Economics, and Technologies. *Joule* **4** (1), 21-32 (2020).
(28) C. L. Camille. Process for the protection of metals against the corrosive action of brines. 1963.
(29) W. B. Murray; R. E. Wright. Corrosion prevention with sodium silicate and soluble zinc salts. 1971.
(30) B. Narayanan; S. A. Deshmukh; S. K. R. S. Sankaranarayanan; S. Ramanathan. Strong correlations between structural order and passive state at water–copper oxide interfaces. *Electrochim. Acta* **179**, 386-393 (2015).
(31) F. W. Starr; J. K. Nielsen; H. E. Stanley. Fast and Slow Dynamics of Hydrogen Bonds in Liquid Water. *Phys. Rev. Lett.* **82** (11), 2294-2297 (1999).
(32) W. Salama; M. El Aref; R. Gaupp. Spectroscopic characterization of iron ores formed in different geological environments using FTIR, XPS, Mössbauer spectroscopy and thermoanalyses. *Spectrochim.* **136**, 1816-1826 (2015).
(33) A. Teterin; N. Kalmykov; P. Novikov; A. Y. Sapozhnikov; L. Vukchevich; Y. A. Teterin; I. K. Maslakov; O. I. Utkin; B. I. Hasanova; S. N. Shcherbina. X-ray photoelectron spectroscopy study of interaction of Np5+ with goethite α-FeOOH. *Nucl. Technol.* **20**, 38-44 (2005).
(34) A. P. Grosvenor; B. A. Kobe; M. C. Biesinger; N. S. McIntyre. Investigation of multiplet splitting of Fe 2p XPS spectra and bonding in iron compounds. *Surf Interface Anal.* **36** (12), 1564-1574 (2004).
(35) T. Yamashita; P. Hayes. Effect of curve fitting parameters on quantitative analysis of Fe0.94O and Fe2O3 using XPS. *J. Electron. Spectros. Relat. Phenomena.* **152** (1), 6-11 (2006).
(36) B. Lesiak; N. Rangam; P. Jiricek; I. Gordeev; J. Tóth; L. Kövér; M. Mohai; P. Borowicz. Surface Study of Fe3O4 Nanoparticles Functionalized With Biocompatible Adsorbed Molecules. *Front. Chem.* **7**, (2019).
(37) T. Misawa. The thermodynamic consideration for Fe-H2O system at 25°C. *Corros. Sci.* **13** (9), 659-676 (1973).
(38) M. J. N. Pourbaix. Atlas of Electrochemical Equilibria in Aqueous Solutions. 1974.
(39) J. K. Nørskov; T. Bligaard; A. Logadottir; J. R. Kitchin; J. G. Chen; S. Pandelov; U. Stimming. Trends in the Exchange Current for Hydrogen Evolution. *J. Electrochem. Soc.* **152** (3), J23 (2005).
(40) A. A. Peterson; F. Abild-Pedersen; F. Studt; J. Rossmeisl; J. K. Nørskov. How copper catalyzes the electroreduction of carbon dioxide into hydrocarbon fuels. *Energy Environ. Sci.* **3** (9), 1311-1315 (2010).
(41) X. Liu; Y. Jiao; Y. Zheng; K. Davey; S.-Z. Qiao. A computational study on Pt and Ru dimers supported on graphene for the hydrogen evolution reaction: new insight into the alkaline mechanism. *J.Mater. Chem. A* **7** (8), 3648-3654 (2019).
(42) B. Zhang; J. Wang; J. Liu; L. Zhang; H. Wan; L. Miao; J. Jiang. Dual-Descriptor Tailoring: The Hydroxyl Adsorption Energy-Dependent Hydrogen Evolution Kinetics of High-Valance State Doped Ni3N in Alkaline Media. *ACS Catal.* **9** (10), 9332-9338 (2019).
(43) A. Mekki; D. Holland; C. F. McConville; M. Salim. An XPS study of iron sodium silicate glass surfaces. *J. Non Cryst. Solids* **208** (3), 267-276 (1996).
(44) A. Mendiboure; C. Delmas; P. Hagenmuller. Electrochemical intercalation and deintercalation of NaxMnO2 bronzes. *J Solid State Chem.* **57**, 323-331 (1985).
(45) S. Plimpton. Fast Parallel Algorithms for Short-Range Molecular Dynamics. *J. Comput. Phy.* **117** (1), 1-19 (1995).

(46) A. P. Thompson; H. M. Aktulga; R. Berger; D. S. Bolintineanu; W. M. Brown; P. S. Crozier; P. J. in 't Veld; A. Kohlmeyer; S. G. Moore; T. D. Nguyen; et al. LAMMPS - a flexible simulation tool for particle-based materials modeling at the atomic, meso, and continuum scales. *Comput. Phys. Commun.* **271**, 108171 (2022).
(47) H. M. Aktulga; J. C. Fogarty; S. A. Pandit; A. Y. Grama. Parallel reactive molecular dynamics: Numerical methods and algorithmic techniques. *Parallel Comput.* **38** (4), 245-259 (2012).
(48) S. H. Hahn; J. Rimsza; L. Criscenti; W. Sun; L. Deng; J. Du; T. Liang; S. B. Sinnott; A. C. T. van Duin. Development of a ReaxFF Reactive Force Field for NaSiOx/Water Systems and Its Application to Sodium and Proton Self-Diffusion. *J. Phys. Chem. C* **122** (34), 19613-19624 (2018).
(49) S. H. Hahn; A. C. T. van Duin. Surface Reactivity and Leaching of a Sodium Silicate Glass under an Aqueous Environment: A ReaxFF Molecular Dynamics Study. *J. Phys. Chem. C* **123** (25), 15606-15617 (2019).
(50) S. Deshmukh; G. Kamath; S. K. R. S. Sankaranarayanan. Effect of Nanoscale Confinement on Freezing of Modified Water at Room Temperature and Ambient Pressure. *ChemPhysChem* **15** (8), 1632-1642 (2014).
(51) S. A. Deshmukh; S. K. R. S. Sankaranarayanan; K. Suthar; D. C. Mancini. Role of Solvation Dynamics and Local Ordering of Water in Inducing Conformational Transitions in Poly(N-isopropylacrylamide) Oligomers through the LCST. *J. Phys. Chem. B* **116** (9), 2651-2663 (2012).
(52) G. Kresse; D. Joubert. From ultrasoft pseudopotentials to the projector augmented-wave method. *Phys. Rev. B* **59** (3), 1758-1775 (1999).
(53) G. Kresse; J. Furthmüller. Efficient iterative schemes for ab initio total-energy calculations using a plane-wave basis set. *Phys. Rev. B* **54** (16), 11169-11186 (1996).
(54) J. P. Perdew; K. Burke; M. Ernzerhof. Generalized Gradient Approximation Made Simple. *Phys. Rev. Lett.* **77** (18), 3865-3868 (1996).
(55) A. I. Liechtenstein; V. I. Anisimov; J. Zaanen. Density-functional theory and strong interactions: Orbital ordering in Mott-Hubbard insulators. *Phys. Rev. B* **52** (8), R5467-R5470 (1995).
(56) S. Grimme; S. Ehrlich; L. Goerigk. Effect of the damping function in dispersion corrected density functional theory. *J. Comput. Chem.* **32** (7), 1456-1465 (2011).